Check for updates

All-optical imaging and manipulation of whole-brain neuronal activities in behaving larval zebrafish

ZHEN-FEI JIAO,[1,5] CHUN-FENG SHANG,[2,5,7] YU-FAN WANG,[2,3,5] ZHE YANG,[1] CHEN YANG,[2] FU-NING LI,[2,3] JIN-ZE XIE,[2,3] JING-WEI PAN,[2] LING FU,[1,6] AND JIU-LIN DU[2,3,4,8]

[1]Britton Chance Center for Biomedical Photonics, MoE Key Laboratory for Biomedical Photonics, Collaborative Innovation Center for Biomedical Engineering, School of Engineering Sciences, Wuhan National Laboratory for Optoelectronics, Huazhong University of Science and Technology, Wuhan, Hubei 430074, China

[2]Institute of Neuroscience, State Key Laboratory of Neuroscience, Center for Excellence in Brain Science and Intelligence Technology, Chinese Academy of Sciences, 320 Yue-Yang Road, Shanghai 200031, China

[3]University of Chinese Academy of Sciences, 19A Yu-Quan Road, Beijing 100049, China

[4]ShanghaiTech University, 319 Yue-Yang Road, Shanghai 200031, China

[5]These authors contributed equally to this work.

[6]lfu@mail.hust.edu.cn

[7]cfshang@ion.ac.cn

[8]forestdu@ion.ac.cn

Abstract: All-optical interrogation of population neuron activity is a promising approach to deciphering the neural circuit mechanisms supporting brain functions. However, this interrogation is currently limited to local brain areas. Here, we incorporate patterned photo-stimulation into light-sheet microscopy, allowing simultaneous targeted optogenetic manipulation and brain-wide monitoring of the neuronal activities of head-restrained behaving larval zebrafish. Using this system, we photo-stimulate arbitrarily selected neurons (regions as small as ~10-20 neurons in 3D) in zebrafish larvae with pan-neuronal expression of a spectrally separated calcium indicator, GCaMP6f, and an activity actuator, ChrimsonR, and observe downstream neural circuit activation and behavior generation. This approach allows us to dissect the causal role of neural circuits in brain functions and behavior generation.

1. Introduction

Large-scale activation of neural circuits across the whole brain is often required to generate animal behaviors [1–4]. Even instinctive behaviors such as prey capture by larval zebrafish involve coordinated functioning of multiple brain areas [5–7]. Therefore, deciphering behavior-relevant neural circuits requires interrogation of neuronal activities across large brain areas, or even the whole brain. The larval zebrafish is an ideal animal model for such studies, because its small and transparent brain is well suited to optical monitoring and manipulation of neuronal activities across the whole brain at single-cell resolution [6,8]. This good candidacy is especially true considering the relatively recent technological advances concerning probes for optical readout and manipulation of neuronal activity [9–12]. Recently, interrogation was attempted using combined point scanning imaging and spatially localized manipulation of the activities of target neurons [13–15]. However, only hundreds of neurons in local brain areas were examined simultaneously, because of the limitation of the point imaging assay [13–15], which prevented examination of brain-wide neural circuits.

In this study, we construct an all-optical system capable of simultaneous imaging and targeted manipulation of neuronal activities across the whole brain in behaving larval zebrafish. A state-of-the-art method of targeted optical manipulation, which is based on beam shaping using a digital micromirror device (DMD) [16–18], is introduced to light-sheet microscopy, which is two orders of magnitude faster than point scanning imaging [19–23]. Combination of the red-shifted activity actuator ChrimsonR and the Ca^{2+} indicator GCaMP6f allows simultaneous manipulation and imaging of neuronal activities with minimal spectral cross-talk [9,10]. In addition, high-speed behavior monitoring is integrated into the system to facilitate study of the neuronal ensembles' roles in behavior generation. As a proof of principle, DMD-based targeted activation of arbitrarily selected neurons is shown to effectively activate synaptic connections and brain-wide downstream neural circuits, and to evoke stereotyped behaviors, demonstrating the capability of our system to aid investigation of the functions of brain-wide neural circuits in small animals.

2. Materials and method

2.1 All-optical imaging and manipulation of whole-brain neuronal activities in behaving larval zebrafish
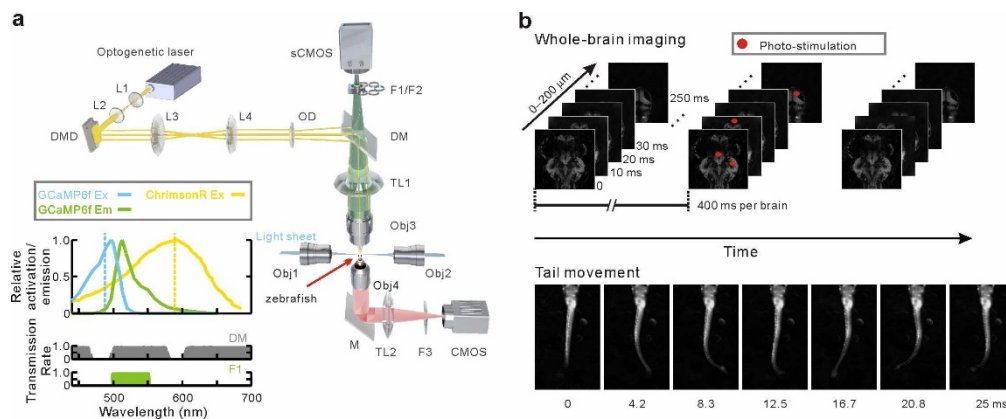

Fig. 1. Simultaneous whole-brain imaging and targeted manipulation of neuronal activity of behaving larval zebrafish. (a) Schematic diagram of setup. Patterned photo-stimulation was incorporated into a light-sheet microscope through the imaging light path, and a near-infrared light path was used for behavior monitoring. (bottom left) GCaMP6f, ChrimsonR, and filter combination spectra. The separated GCaMP6f and ChrimsonR spectra allowed simultaneous light-sheet imaging and photo-stimulation without spectral bleeding. ChrimsonR Ex: ChrimsonR excitation spectrum; GCaMP6f Ex and Em: GCaMP6f excitation and fluorescence emission spectra, respectively. Blue and yellow dashed lines: GCaMP6f (488 nm) and ChrimsonR (589 nm) excitation wavelengths, respectively. (b) Simultaneous targeted manipulation and whole-brain imaging of neuronal activity (top) and behavior monitoring (bottom). Distributed neurons were targeted with photo-stimulation (red dots) during whole-brain neuronal activity imaging and fish behavior monitoring. (DMD: digital micromirror device; L1−L4: lenses 1−4; OD: optical diffuser; (s)CMOS: (scientific) complementary metal-oxide semiconductor; F1, F2: green and red band-pass filters, respectively; F3: infrared long-pass filter; DM: multi-band dichroic mirror; TL1, TL2: tube lenses 1 and 2; Obj3, Obj4: fluorescence detection and behavior monitoring objectives, respectively; M, reflective mirror.)

We constructed a setup for dissecting the causal role of functional neuronal ensembles in neural functions and behavior generation of zebrafish larvae (Fig. 1(a)). In detail, we customized a light-sheet microscope to record brain-wide neuronal activities and introduced patterned photo-stimulation for simultaneous optogenetic manipulation of arbitrarily selected neurons across the whole brain. This combination was achieved through fine alignment of the optics and precise synchronization of the instruments. First, we combined the photo-stimulation light path with the light-sheet imaging by sharing the fluorescence detection

objective (Obj3; W N-Achroplan 20 × /0.5, Carl Zeiss), tube lens (TL1; #58-395, Zeiss), and multi-band dichroic mirror (DM; Di01-R405/488/594, Semrock) (Fig. 1(a)). The chips of the imaging camera (scientific complementary metal-oxide semiconductor (sCMOS); Orca Flash 4.0, Hamamatsu Photonics) and the DMD were aligned to be conjugated with the Obj3 focal plane and registered pixel by pixel. Second, we inserted an optical diffuser (OD; #48514, Edmund) conjugated with both the DMD and the Obj3 focal plane. Third, the DMD and sCMOS were synchronously triggered by a high-speed data acquisition (DAQ) card to ensure simultaneous imaging and photo-stimulation. Another DAQ card was then used to record the trigger-out signals from the sCMOS and DMD, to verify the synchrony. Finally, we used a high-speed CMOS (GO 5000, JAI, 240 Hz) to monitor the tail movement of head-restrained larval zebrafish with near-infrared illumination (Fig. 1).

By integrating imaging, photo-stimulation, and behavior monitoring, we could target arbitrarily selected neurons at different lateral and axial positions with photo-stimulation, while simultaneously performing continuous volumetric imaging of the whole-brain neuronal activities and behavior monitoring. This is shown for a larval zebrafish (5 days post-fertilization, dpf) in Fig. 1(b).

2.2 Zebrafish husbandry

Adult zebrafish (*Danio rerio*) were maintained at the National Zebrafish Resources of China facility (NZRC, Shanghai, China) at 28 °C. Embryos were raised under a 14−10-h light-dark cycle in 10% Hanks' solution consisting of (in mM): 140 NaCl, 5.4 KCl, 0.25 Na_2HPO_4, 0.44 KH_2PO_4, 1.3 $CaCl_2$, 1.0 $MgSO_4$, and 4.2 $NaHCO_3$ (pH 7.2), and treated with 0.003% 1-phenyl-2-thiourea (PTU, Sigma) from 24 h post-fertilization to prevent pigment formation. Larvae at 4–9 dpf were employed in the experiments. All the experimental protocols were approved by the Animal Use Committee of the Institute of Neuroscience, Chinese Academy of Sciences.

2.3 Transgenic zebrafish lines

For simultaneous Ca^{2+} imaging and optogenetic manipulation, it is critical that the Ca^{2+} indicator and the optogenetic actuator have separate activation spectra. As GCaMP6f [9], a fast and sensitive Ca^{2+} indicator, was used for Ca^{2+} imaging, we chose the red-shifted optogenetic actuator ChrimsonR [10] for optogenetic manipulation, because its activation peak is well beyond both the excitation and emission spectra of GCaMP6f (Fig. 1(a, bottom left)). Therefore, to monitor and optogenetically manipulate neuronal activities across the whole brain, we used the double transgenic zebrafish line *Tg(elavl3:H2B-GCaMP6f;elavl3:ChrimsonR-tdTomato)*, for which most neurons in the brain express both GCaMP6f and ChrimsonR driven by the pan-neuronal promoter *elavl3* [24].

Tg(elavl3:H2B-GCaMP6f;elavl3:ChrimsonR-tdTomato) was generated by crossing *Tg(elavl3:H2B-GCaMP6f)* and *Tg(elavl3:ChrimsonR-tdTomato)*. The former was from the Ahrens Lab at Janelia Research Campus and the latter was generated in an albino background using *Tol2* transposon. The *ChrimsonR-tdTomato* fusion gene was obtained from *386-pCAG-ChR88m19-tdTomato* (Addgene plasmid #59169) and sub-cloned into a *Tol2* vector that contained the zebrafish *elavl3* promoter at XhoI/NotI sites. The transgene construct and transposase mRNA were co-injected into the embryos at the one-cell stage, and the transgenic lines were screened out. The *Tg(hspGFF62A;UAS:GFP)* line in which the Mauthner cells express Gal4 at a high level was from the Kawakami Lab at the National Institute of Genetics, Japan. To express ChrimsonR in Mauthner cells, a plasmid of *UAS:ChrimsonR-tdTomato* was injected into one-cell stage embryos. The *UAS:ChrimsonR-tdTomato* was constructed by sub-cloning the *ChrimsonR-tdTomato* fusion gene into a *Tol2* vector containing 14 × UAS.

2.4 Light-sheet imaging

For light-sheet imaging, a blue laser beam (Sapphire LP 488 100 CW, Coherent) was intensity-modulated by an acousto-optic modulator (AOM; AOMO 3080-125, Gooch & Housego), expanded by a beam expander (BE05M-A, Thorlabs), and projected onto two orthogonal galvano mirrors (6215H, Cambridge). The laser beam was then directed into an F-theta lens (#63-310, Edmund Optics), forming a planar scanning optical field. A 50/50 beam splitter (BS013, Thorlabs) positioned after the F-theta lens divided the beam in two, with each component then being re-imaged by an illumination tube lens (LA1979, Thorlabs) and a low-numerical-aperture (NA) illumination objective (GCO-2101 4 × , NA 0.1, China Daheng Group) into the sample space, generating bilateral scanning light-sheets. Light sheets (4.8-μm waist thickness, 1.7-mm horizontal scanning width) were generated by a horizontal galvano mirror (Galvo XY) that quickly scanned the laser beam in the horizontal plane. A vertical galvano mirror (Galvo Z) scanned the light sheets perpendicularly for optical sectioning of the specimen. Obj3 was scanned axially by an objective piezo positioner (P-725.2CD, Physik Instrumente) to collect the fluorescence emitted at different imaging depths. The light-sheet and Obj3 scanning procedures were set synchronously in the control program. The collected fluorescence was imaged by Obj3 and TL1, filtered by the DM and a green band-pass filter (F1; FF01-525/50, Semrock), and captured by the sCMOS (Fig. 1(a)). The ChrimsonR expression was examined by considering the fluorescence of tdTomato, which was fused with ChrimsonR, using green light sheets (laser: OBIS 561 nm LS 100 mW, Coherent) and a red band-pass filter (F2; FF01-609/57, Semrock). The blue and green laser beams were combined by a dichroic mirror (FF506-Di03, Semrock).

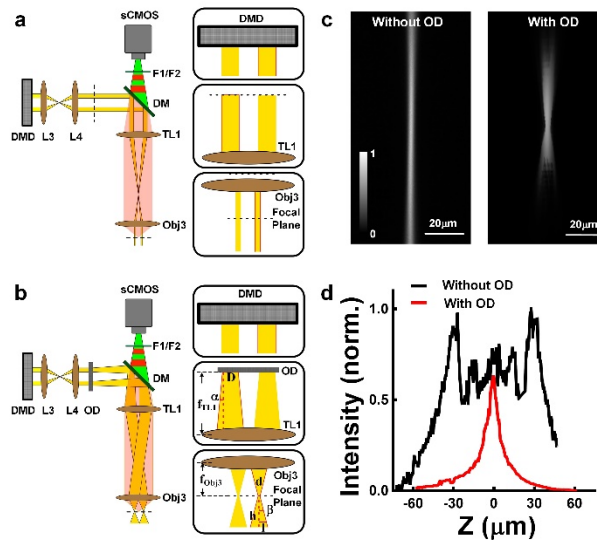### 2.5 Combination of DMD-based photo-stimulation and light-sheet microscopy

Fig. 2. Axial resolution of OD-enhanced photo-stimulation. (a and b, left) Optical layout of DMD integration into light-sheet microscope without (a) or with (b) OD. An intensity-modulated beam was relayed by a lens pair (L3–L4) arranged in 4*f* to the dashed plane or the OD after L4. The beam from the dashed plane or OD was reflected by the DM to the TL1 and Obj3 of the light-sheet microscope. The Obj3 focal plane was conjugated with the dashed plane or OD. (a and b, right) Magnified image of DMD, dashed plane or OD before TL1, and focal plane after Obj3. (c) Axial section of photo-stimulation beam measured without (left) or with OD (right) using behavior-monitoring light path. (d) Axial resolution of photo-stimulation without (black curve) and with (red curve) an OD, being 72.6 or 19.6 μm, respectively.

An amber laser beam (MGL-W-589nm-2W, Changchun New Industries) was employed to activate ChrimsonR. To fill the DMD chip (16-mm diagonal, V4100 module with 0.7" extended graphics array for visible light; Texas Instruments), the beam was expanded by a lens pair (L1–L2; f_{L1} = 60 mm, f_{L2} = 300 mm, where f represents focal length and the subscript indicates the corresponding lens) arranged in $2f_{L1} + 2f_{L2}$. The DMD-patterned beam was relayed to the OD (diameter = 50 mm) by another lens pair (L3–L4; $f_{L3} = f_{L4}$ = 75 mm) arranged in $4f$. The laser beam was diffused by the OD, forming a divergent beam, and re-imaged to the Obj3 focal plane (Figs. 1(a) and Fig. 2).

2.6 Optical diffuser enhancement of photo-stimulation axial resolution

The DMD array consisted of 1024 × 768 micromirrors, each of which could be individually turned on and off using a high-speed controller suite (ALP-4.2, ViALUX), thus patterning the laser-power spatial distribution. However, a collimated photo-stimulation beam induced axially non-selective activation around the target neurons (Fig. 2(a)). To achieve more precise photo-stimulation in a confined volume, an OD was used to generate a divergent beam along the axial axis, so as to reduce the intensity of the photo-stimulation beam outside the imaging focal plane. The DMD chip and OD were conjugated using a lens pair ($f_{L3} = f_{L4}$ = 75 mm) arranged as a $4f$ system (Fig. 2(b)). The magnification M of the light-sheet imaging could be expressed as

$$M = \frac{f_{TL1}}{f_{Obj3}},\qquad(1)$$

where f_{TL1} and f_{Obj3} are the focal lengths of TL1 and Obj3, respectively. Thus, the divergent beam after the OD was re-imaged by TL1, and Obj3 and could be expressed as

$$d = \frac{D}{M},\qquad(2)$$

$$\tan(\beta) = M \tan(\alpha),\qquad(3)$$

where d and β are the reimaged beam diameter and angle, D and α are the diameter and diffusing angle of the patterned beam on the OD, respectively, while the beam is at the Obj3 focal plane.

At the out-of-focal plane, where the optical intensity decreased to half that at the focal plane, the beam radius l could be expressed as

$$l = \frac{\sqrt{2}}{2}d.\qquad(4)$$

The distance h of this plane to the focal plane was determined as

$$h = \frac{(l - d/2)}{\tan(\beta)} = \frac{(l - d/2)}{M \tan(\alpha)}.\qquad(5)$$

Here, $2h$ was defined as the axial resolution of the photo-stimulation. Note that $2h$ can be improved by using an OD with a larger diffusing angle. However, as the Obj3 pupil size is finite (approximately 10 mm), a larger diffusing angle would yield reduced photo-stimulation power after the Obj3.

Next, we designed experiments to quantify the photo-stimulation axial resolution with or without the OD. First, a target disk pattern with D = 100 μm was loaded onto the DMD (Figs. 2(a) and 2(b)). Then, we measured the intensity profile of the Obj3 focal volume by axially scanning a high-NA objective (Olympus, LUMPLELN-PLAN, 60 × /1.0) mounted on the

behavior monitoring system with a 1-μm step. The axial resolutions of the stimulation, as characterized by the full-width at half maximum (FWHM) of the stimulation beam intensity, were 72.6 and 19.6 μm when the OD flipped down and up, respectively. These results are consistent with the theoretical calculations (Fig. 2(d) black and red curve).

2.7 Pipeline for photo-stimulation of targeted neurons

To generate appropriate patterns for targeted photo-stimulation, we first chose target neurons in fluorescence images captured with the sCMOS (Figs. 3(a) and 3(b)). Each sCMOS image corresponded to an area of the same size on the DMD plane, because the sample space was projected onto both the sCMOS and DMD chips with the same magnification. Then, we linearly transformed the original sCMOS image (2048 × 2048 pixels) into a temporary image (978 × 978 pixels) based on the different pixel sizes (6.5 and 13.6 μm for the sCMOS and DMD, respectively). However, the DMD chip was longer (13.9 mm) and narrower (10.4 mm) than the sCMOS chip (length and width both 13.3 mm). Thus, we added 46 marginal pixels to the temporary image in one dimension and removed 210 pixels from the other dimension to obtain the DMD pattern (1024 × 768 pixels). Note that the image was rotated because of the different orientations of the DMD and sCMOS in our system (Fig. 3(c)).
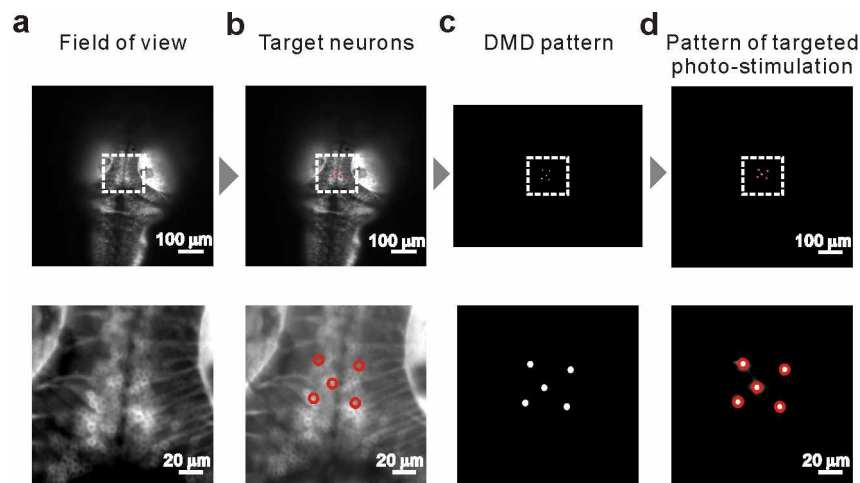

Fig. 3. Pipeline for photo-stimulation of targeted neurons. From the captured fluorescence image of the brain of a 5-dpf zebrafish larva pan-neuronally expressing *ChrimsonR-tdTomato* (a), we arbitrarily selected single neurons (red circles in (b)) as photo-stimulation targets. Based on these neurons' positions and soma sizes, we calculated the photo-stimulation pattern and loaded it onto the DMD (c) to activate the target-corresponding micromirrors. Upon this targeted photo-stimulation, tdTomato fluorescence was imaged from the same field of view as for (a), and fluorescence was observed on the target neurons. (a and d, bottom) Enlarged view of region of interest (white dashed square) in each panel.

2.8 Behavior monitoring

For behavior monitoring, the zebrafish larva was restrained by low-melting point agarose (1.2%, in Hanks' solution; Invitrogen) in a dorsal-up position in a home-designed chamber in which its tail could freely move. The chamber had two glass windows on the left and right for light-sheet propagation, and a third at the bottom for behavior monitoring. Under near-infrared illumination (WFA1020, Thorlabs), the behavior monitoring objective (Obj4, RMS4X, Olympus) and a plano-convex lens (LA1433-A-ML, Thorlabs) imaged the fish onto the CMOS, which was mounted with a long-pass filter (GCC-300601, China Daheng Group) (Fig. 1(a)). Images were taken at 240 Hz to capture the fine details of the larval behavior.

2.9 System control for simultaneous imaging, targeted photo-stimulation, and behavior monitoring

The instruments in the system were orchestrated by a high-speed DAQ Card (PCI-6733, National Instruments), the sampling rate of which was approximately 20 times higher than the refresh rate of the galvano mirrors, which were the fastest instruments in our system. Using a customized LabView controller (LabView 2012, National Instruments), trigger signals were synchronized to achieve photo-stimulation and imaging. The trigger-out signals of the sCMOS and DMD were recorded with another high-speed input/output device (National Instruments, USB-6363).

Simultaneous light-sheet imaging and targeted photo-stimulation were performed either at a single plane or across a volume according to different experimental situation. The single-plane mode was employed to characterize the photo-stimulation performance with 10ms pulsed photo-stimulation, 0.5s duration and 50fps imaging rate. A continuous transistor-transistor logic (TTL) signal was used to trigger exposure of the sCMOS, and another TTL signal was used to schedule the pulsed photo-stimulation. In the volumetric mode, the light-sheets and Obj3 were synchronously scanned up and down along the dorsal-ventral axis. The whole-brain imaging was as fast as 2.5 volumes/s, and covered an axial depth of 200 μm with an 8-μm step. To stimulate target neurons at each imaging depth, the system was updated with different DMD photo-stimulation patterns to ensure precise photo-stimulation location. For instance, if the targeted neurons spanned three imaging depths and different spatial locations, the corresponding DMD patterns were loaded on and changed to achieve accurate but alternative photo-stimulation patterns across different planes. In the volumetric mode, photo-stimulation duration on each plane equals to the sCMOS exposure time (~10ms, Fig. 4) Behavior monitoring data were acquired at 240 Hz with a TTL signal as the frame trigger.
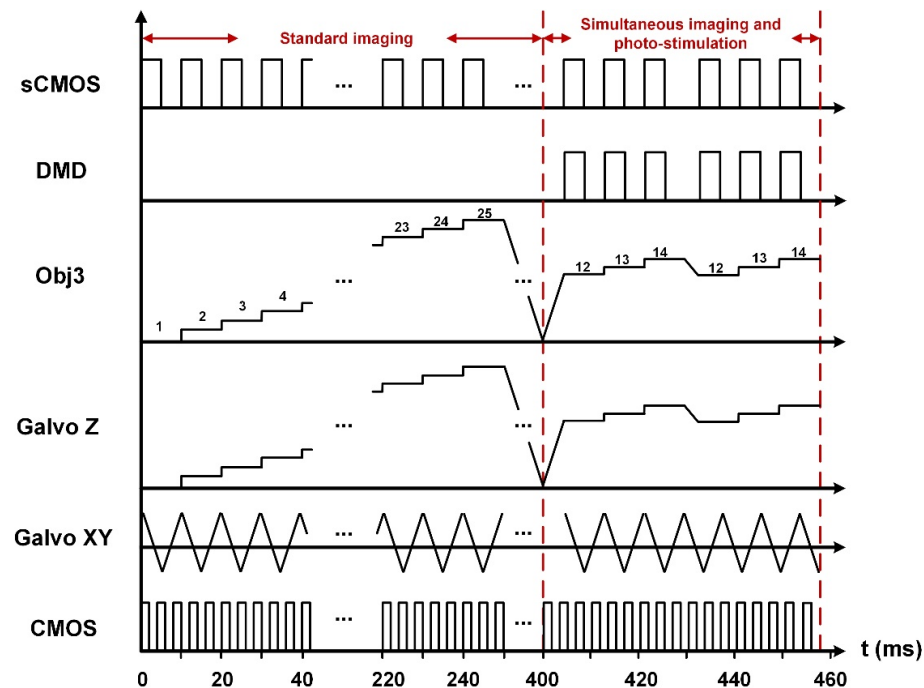

Fig. 4. Timing diagram of control waveforms for all instruments during simultaneous volumetric imaging and targeted photo-stimulation. All signals were generated by a PCI-6733 data acquisition (DAQ) card programmed by a LabView controller. (Galvo XY and Z: horizontal and vertical galvano mirrors, respectively.)

2.10 Image acquisition and processing

Fluorescence images were captured by the sCMOS under the control of HCImage software (4.2.0.33, Hamamatsu) and directly stored in binary files in a redundant array of independent disks (RAID) 0 array of solid-state hard discs (SSD PM871, SAMSUNG). The data were loaded into Matlab through a mex file. The images were nonlinearly registered layer-by-layer to an averaged reference volume [8] and the neurons were segmented from the registered results using a water-shed algorithm. Fluorescence-signal time series were measured for each segmented neuron and normalized to an order-filtered baseline (10-s window, 20%). The background noise of the sCMOS was removed from the fluorescence before normalization.

2.11 Statistical analysis

Spearman's correlation was employed to assess the variation of the photo-stimulation beam diameter over the imaging depth. This assessment was implemented using Matlab script.

Neuronal responses to photo-stimulation were considered significant if the Ca^{2+} activity in the first second after photo-stimulation was continuously and significantly higher than the pre-stimulation activity (twice the standard deviation higher than the mean or more). The Ca^{2+} activity was measured as the ratio of the GCaMP6f fluorescence change ΔF to the basal fluorescence F_0. Neurons showing significant responses to at least three of four repeated photo-stimulations were considered reliably responsive. The statistical data were presented as mean ± standard error of mean (SEM) values.

3. Results

3.1 Light-sheet microscope performance

The field of view was $692 \times 692 \times 200 \ \mu m^3$, covering almost the whole brain of a larval zebrafish. The lateral and axial resolutions were 0.8 and 5.0 μm, respectively (Fig. 5). Volumetric imaging was acquired section by section with an 8-μm step at 2.5 volumes/s (Fig. 1(b)).
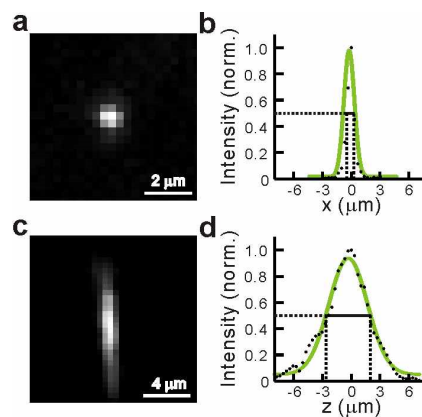

Fig. 5. Spatial resolution of light-sheet microscope. (a, b) Lateral spatial resolution of light-sheet microscope, examined by measuring point-spread-function full width at half maximum (FWHM) and Gaussian fitting (green line in (b)). Fluorescent beads with 20-nm diameter (F8787, ThermoFisher) were illuminated by the light sheets and employed as a point light source. The fluorescence intensity profile showed an FWHM of 0.8 μm. This lateral resolution was sufficient to discriminate the cell contour. (c, d) Axial resolution of light-sheet microscope, measured by axially scanning the fluorescent beads and capturing images at various axial distances. The measured axial resolution was approximately 5.0 μm. This is consistent with the calculated light-sheet thickness (4.8-μm FWHM at waist) and the calculated Obj3 axial resolution (5.0 μm).

3.2 Targeting performance of patterned photo-stimulation

Targeted photo-stimulation was achieved by shaping the stimulation beam according to the spatial positions of individual target neurons in the brain. Note that both precise positioning and low scattering of the photo-stimulation beam are critical for target manipulation. To calibrate the targeting performance, we used *Tg(elavl3:ChrimsonR-tdTomato)* larvae, because tdTomato can be excited by the 589-nm light used to activate ChrimsonR (Fig. 6). We selected single neurons in the zebrafish brain from the fluorescent images and patterned the photo-stimulation based on the DMD pixel registration to the sCMOS (Fig. 3 and Fig. 7(a)). Neurons with diameters of 4.6 ± 0.2 μm ($n = 71$) were targeted at various depths below the dorsal brain surface (up to 190 μm). The emitted fluorescence of tdTomato was collected by the sCMOS through a long-pass filter (F4; FELH0600, Thorlabs), while the excitation light was filtered out (Fig. 6). We observed that the emitted fluorescence of tdTomato was restricted to the target area with a mean deviation of 0.3 μm (first quantile, −0.2 μm, third quantile, 0.6 μm, 608 neurons in 5 larvae). The photo-stimulation beam diameter after light scattering in the larval zebrafish, which was characterized by the lateral FWHMs of the fluorescence intensity profiles of the targeted neurons, was 10.1 ± 0.1 μm (Fig. 7(b)) and covered 9 ± 1 cells (in 5 larvae). Considering the axial FWHM (19.6 μm) of the photo-stimulation beam (Fig. 2(d)), the target regions were as small as ~10-20 neurons in 3D. The photo-stimulation beam diameter was slightly correlated with the penetration depth (9.4 ± 0.6 μm at the dorsal brain surface, 11.4 ± 0.7 μm at 190 μm below the dorsal surface; Spearman's correlation, $\rho = 0.2$, $P < 0.001$; Fig. 7(c)).
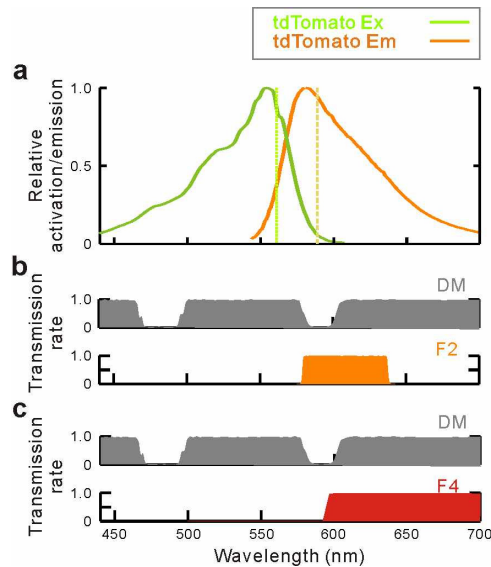

Fig. 6. Spectra and filter combinations for tdTomato fluorescence examination. (a) Excitation (tdTomato Ex) and fluorescence emission (tdTomato Em) spectra of tdTomato. The green and yellow dashed lines indicate 561 and 589 nm, respectively. (b) Filter combination for examining tdTomato fluorescence to assess ChrimsonR expression. As ChrimsonR does not emit fluorescence, we assessed its expression in targeted neurons by examining the tdTomato expression, which was fused with ChrimsonR. Light sheets with 561-nm wavelength (green dashed line in (a)) were employed to excite tdTomato and the emitted fluorescence was filtered by DM and F2 before being captured by the sCMOS. (c) Filter combination for examining tdTomato to characterize photo-stimulation performance. Patterned photo-stimulation of 589 nm (yellow dashed line in (a)) was targeted towards single neurons expressing tdTomato. The emitted fluorescence was filtered by DM and F4, before being captured by the sCMOS. A filter wheel was used to switch filters in experiment.

A scattered laser may activate cells near the target neurons and impair the photo-stimulation spatial precision. To examine this behavior, we targeted a single neuron, 8ms pulsed photo-stimulation in 0.5s duration with 50fps imaging rate, in the optic tectum (OT) of a sample *Tg(elavl3:H2B-GCaMP6f;elavl3:ChrimsonR-tdTomato)* larva at 9 dpf. We observed that the target as well as 5 nearby neurons within 15 μm of the target were reliably activated (Figs. 7(d) and 7(e)), consistent with the photo-stimulation beam diameter. The optogenetic response amplitude showed a decreasing trend with increased target distance (Fig. 7(f)), attributable to the decreasing power intensity of the scattered laser. To exclude the possible interference of laser-evoked visual responses and synaptic transmission, we performed bilateral enucleation and blocked glutamatergic synaptic transmission through bath application of 6-cyano-7-nitroquinoxaline-2,3-dione (CNQX; 50 μM) and DL-2-amino-5-phosphonovaleric acid (APV; 50 μM), antagonists of the α-amino-3-hydroxy-5-methyl-4-isoxazolepropionic acid subtype and the N-methyl-D-aspartate subtype of glutamate receptors, respectively. The lack of ideal single-neuron targeting could be attributed to the distorted laser beam due to tissue-scattering, uneven expression of ChrimsonR among the neurons, and/or activation of bypassing neuronal processes.
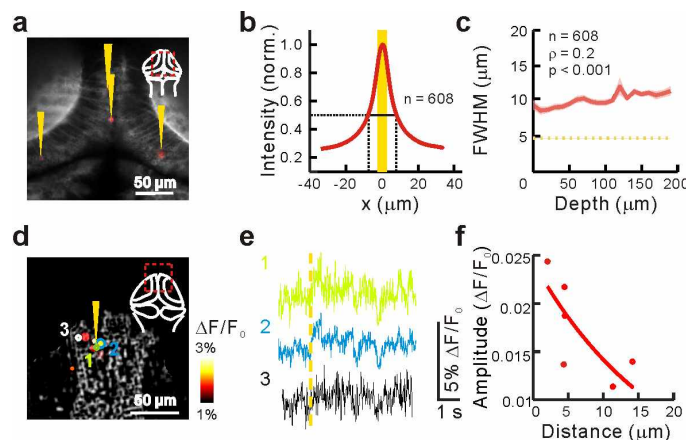

Fig. 7. Targeting performance of patterned photo-stimulation in zebrafish brain. (a) Characterization of photo-stimulation precision in 6-dpf *Tg(elavl3:ChrimsonR-tdTomato)* larva. Single neuron-shaped laser beams (589 nm, yellow triangles) were projected into the larval brain to excite tdTomato and the emitted fluorescence was detected (red, collected at 600 nm and above). Inset: Imaging area position in brain. (b) Photo-stimulation deviation and scattering. Results from 608 cells in 5 larvae were averaged. The shaded box marks the photo-stimulation target range. The tdTomato-emitted fluorescence pattern was fitted with a 2-D Gaussian function. The center position of the fitted fluorescence distribution was compared with that of the target to determine the targeting error, which on average was 0.3 μm (first quartile −0.2 μm, third quartile 0.6 μm). The FWHM of the intensity profile indicates the photo-stimulation beam diameter. (c) Relationship between FWHM and axial depth. The FWHM was slightly correlated with the penetration depth ($n = 608$, $\rho = 0.2$, $P < 0.001$, Spearman's correlation). Yellow line: original photo-stimulation beam diameter; shaded area: mean ± standard error of mean (SEM). (d–f) Example of targeted photo-stimulation precision. Photo-stimulation (10-ms pulses, 0.5-s duration, 50 Hz; yellow triangle in (d) and yellow dashed line in (e)) was targeted towards a single optic tectum (OT) neuron and activated both the target and 5 nearby cells in a 9-dpf *Tg(elavl3:H2B-GCaMP6f;elavl3:ChrimsonR-tdTomato)* larva with bilateral enucleation. Bath application of 6-cyano-7-nitroquinoxaline-2,3-dione (CNQX; 50 μM) and DL-2-amino-5-phosphonovaleric acid (APV; 50 μM) was used to block glutamatergic transmission. The mean optogenetic responses of the target neuron (1), a neighbor neuron (2), and a distant neuron (3, 25 μm from the target) are shown in (e). (f) For the activated neurons, the activation amplitude was lower for the neurons farther from the target. Inset in (d): Imaging area position, the tectal paraventricular zone, in brain. Color bar: change in fluorescence $\Delta F/F_0$. Shaded area: mean ± SEM.

3.3 Targeted photo-stimulation evokes synaptic transmission

The left and right dorsal habenulae (Hb-l and Hb-r, respectively) are connected through commissural fibers [25–27]. To demonstrate the effectiveness of our targeted photo-stimulation as regards synapse activation, we photo-stimulated 9 separate Hb-l neurons (sapnning 24 μm axially) at 25 Hz for 0.72 s, and performed volumetric imaging at 4 Hz spanning almost the whole brain in a 6-dpf *Tg(elavl3:H2B-GCaMP6f;elavl3:ChrimsonR-tdTomato)* larvae. The volumetric imaging was swichted to 25 Hz and was limited to the targeted depths during the stimulation due to the design limit of our system. An example is shown in Fig. 8, in which a cluster of neurons in Hb-l were photo-stimulated. Here, not only the target and 55 nearby neurons in Hb-l, but also 11 neurons in Hb-r were reliably activated. The activities of the contralateral Hb-r neurons were not due to photo-stimulation laser-evoked visual responses, because bilateral enucleation was performed before the experiment. Furthermore, the Hb-r neuron activities were abolished by bath incubation of CNQX (50 μM) and APV (50 μM) (Fig. 8(b, right)). Therefore, DMD-based targeted photo-stimulation can effectively trigger synaptic transmission.
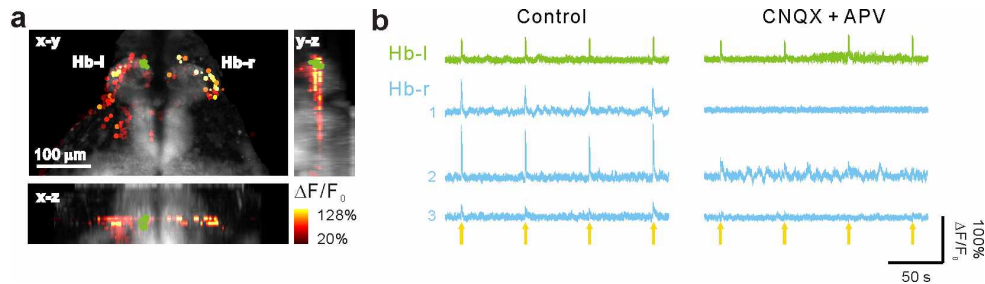

Fig. 8. Targeted photo-stimulation of habenulae evokes synaptic transmission. (a) Postsynaptic responses evoked by targeted photo-stimulation. Nine neurons (green) in the left dorsal habenula (Hb-l) and activated neurons (color dots) in bilateral Hb (55 Hb-l and 11 Hb-r (the right dorsal habenula)) in a *6-dpf Tg(elavl3:H2B-GCaMP6f;elavl3:ChrimsonR-tdTomato)* larva were targeted for photo-stimulation. The neuronal activities were measured based on the amplitude of the GCaMP6f fluorescence change ($\Delta F/F_0$) and superimposed on reference anatomy (grey) in dorsal (x-y), sagittal (y-z) and coronal (x-z) projections. (b) Representative neuronal responses evoked by targeted photo-stimulation before (left) and after (right) blockade of glutamatergic transmission through bath application of CNQX (50 μM) and APV (50 μM). The green traces indicate the response of a targeted neuron in Hb-l, and the blue traces display the postsynaptic responses of three activated neurons in Hb-r. The yellow arrows indicate the targeted photo-stimulation events.

3.4 Targeted photo-stimulation activates brain-wide functional connections

To further demonstrate the capability of targeted photo-stimulation for activating brain-wide downstream neural networks, we patterned photo-stimulation according to the specific anatomical position of the left tegmentum (Teg-l) at each depth (24 μm in total) and applied the patterned photo-stimulation at 25 Hz for 0.72 s in a zebrafish larva with bilateral enucleation. Volumetric imaging was performed at 4 Hz spanning almost the whole brain, but swichted to 25 Hz and was limited to the Teg-l containing depths during the stimulation. (Fig. 9(a)). In the target area, 59% of neurons were reliably activated. Beyond the target area, evoked neuronal activities were observed extensively in various brain regions, including the bilateral pallium (Pa), Hb, thalamus (Th), and OT, as well as the preferentially ipsilateral cerebellum (Cb) and hindbrain (Hind) (Figs. 9(a)-9(c)). Such diverse connections with sensory and motor systems are consistent with previous anatomical studies on teleosts and rodents [28–33]. As an interface for sensorimotor transformation [34–36], the tegmentum is involved in various behaviors that may require its intensive interaction with downstream regions. The ipsilateral-biased innervation of the motor areas, including the Cb and Hind, is also consistent with a premotor role. Note that the OT contained the most activated neurons

among the downstream regions, and the Hb neurons were activated more strongly and at a later stage than the other regions, suggesting the possibility of different circuit connections and functional roles (Figs. 9(b) and 9(c)).
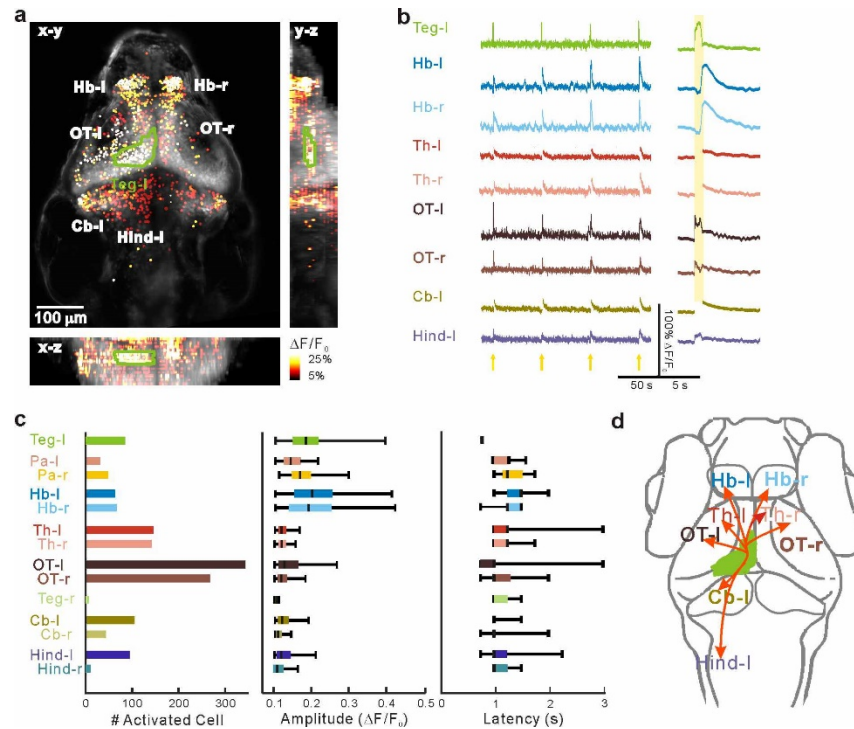

Fig. 9. Targeted photo-stimulation of tegmentum activates brain-wide functional connections. Representative images (a) and traces (b) showing activation of brain-wide downstream neurons evoked by targeted photo-stimulation. The left dorsal tegmentum (Teg-l, green area) in a 6-dpf *Tg(elavl3:H2B-GCaMP6f;elavl3:ChrimsonR-tdTomato)* larva was targeted for photo-stimulation, which activated widely distributed neurons in brain regions including Teg-l, Pa-l, Pa-r, Hb-l, Hb-r, Th-l, Th-r, OT-l, OT-r, Cb-l, and Hind-l (Pa: bilateral pallium; Th: thalmus; CB: cerebellum; Hind: hindbrain). The stimulation pattern designed based on the anatomical position of Teg-l on each depth. (b, right) Average responses expanded in time. The yellow arrows (b, left) and shaded area (b, right) indicate the targeted photo-stimulation events. The activities of the representative Th-l, Th-r, and Cb-l neurons were not recorded during the stimulation with the current experiment paradigm. (c) Activated neuron distribution (left) and differences in optogenetic response amplitude (middle) and latency (right) among regions across the whole brain. Neurons showing significant responses to three or four of four photo-stimulation repetitions were considered reliably responsive and included in the distribution. Box-and-whisker plots of the amplitude and latency represent the 25th, 50th, and 75th quartiles (box lines) and the extreme values (by whiskers). (d) Schematic showing brain-wide functional neural networks downstream of Teg-l. The red arrows represent the functional connections between Teg-l and the indicated brain areas.

3.5 Targeted photo-stimulation evokes behaviors

To demonstrate the influence of targeted photo-stimulation on behaving animals, we freed the tail of a head-restrained larva and optogenetically activated the Mauthner cells, a pair of giant reticulospinal neurons bilaterally located at rhombomere 4 of the hindbrain. The Mauthner cells are motor-command-like neurons for C-start escape behaviors [37–39]. We measured the tail deviation angle from the resting direction (Fig. 10(a)). We transiently expressed *ChrimsonR-tdTomato* in bi- or uni-lateral Mauthner cells in the transgenic line *Tg(hspGFF62A;UAS:GFP)*, and photo-stimulated ChrimsonR-positive Mauthner cells at 100 Hz for 1 s (Fig. 10(b)). This targeted photo-stimulation reliably evoked tail curling to the

contralateral side (5 cells from four fish, Figs. 10(c) and 10(f)), similar to Mauthner-cell-initiated startle responses [38,39]. As a control, photo-stimulation of the Mauthner cells expressing GFP but not ChrimsonR could not evoke tail curling (6 cells from three fish, Figs. 10(d) to 10(f)). To avoid visual-mediated response, the employed larval zebrafish received bilateral enucleation and recovered before the experiment.
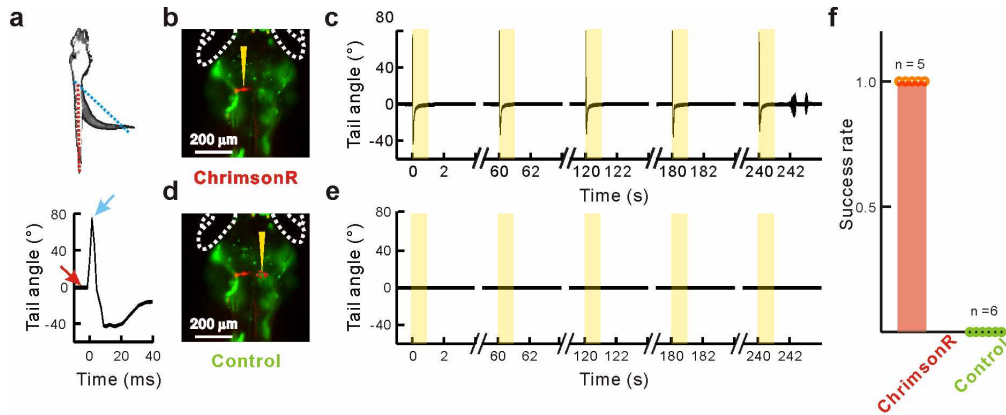

Fig. 10. Targeted photo-stimulation of Mauthner cells evokes tail curling in larval zebrafish. (a) Tail movement of head-restrained larval zebrafish measured in terms of angle between current tail direction (blue) and resting tail position (red). (b, c) Example showing that targeted photo-stimulation (b, yellow triangle) of ChrimsonR-expressing Mauthner cell (b, red) reliably evoked tail curling in five consecutive trials (c). White dashed lines in (b): eye outlines; yellow shaded areas in (c), photo-stimulation periods. (d, e) Example showing that targeted photo-stimulation (d, yellow triangle) of contralateral Mauthner cell (d, red dash circle) with expression of GFP but not ChrimsonR could not evoke tail movement (e). The data shown in (b)–(e) were obtained from the same larva. (f) Success rates of tail movements evoked by targeted photo-stimulation of unilateral Mauthner cells with (red) and without (green) ChrimsonR expression. The numbers indicate the number of examined cells.

4. Discussion

The method presented in this study provides an efficient approach to brain-wide targeted perturbation with simultaneous imaging of neuronal activities. This is critical for elucidating brain-wide neural circuit mechanisms supporting animal behaviors, because behavior-associated neuronal ensembles are usually distributed across many brain areas [1–7]. Targeted optogenetic manipulation improves the specificity of the activity perturbation, from neurons sharing common genetic markers to arbitrarily selected neuronal ensembles that are functionally related and widely distributed [40,41]. Recently, targeted photo-stimulation has been combined with simultaneous activity imaging of dozens to hundreds of neurons in a local brain area [13–15,42]. Although a previous attempt was made to integrate targeted optogenetics with two-photon imaging of an area covering the majority of the midbrain and hindbrain of a larval zebrafish, the limited imaging velocity (4 frames per second and less than 0.4 Hz for volumetric imaging) prevented monitoring of the fast dynamics of the neuronal activities in response to the targeted photo-stimulation [15]. With our system, however, brain-wide neuronal activities can be monitored at 2.5 to 4 Hz, and dynamics in response to targeted photo-stimulation can be examined across the whole brain. For example, in this study, habenular neurons were activated later than tectal and cerebellar neurons (see Fig. 9(b), right), suggesting different dynamic properties of the synaptic connections.

A drawback of photo-stimulation using visible light in zebrafish larva is that visual response may be evoked together with the optogenetic response. To demonstrate the capability of our system we performed bilateral enuleation to rule out the possible visual interference. Such preparation can be employed in future experiments exploring the causal effect of the targeted neurons on the brain-wide downstream. To study physiological

functions requiring intact eyes, visual responses may be suppressed by adaptation to a constantly displayed amber light.

The spatial resolution was limited to a small volume as small as ~10-20 neurons in 3D in our current results. While it is feasible to dissect the brain-wide connection between brain areas, the specific contribution of single neurons could be examined by expressing the rhodopsins sparsely.

The developed system can be further improved in several ways. First, to capture the dynamics of neuronal activities at a higher temporal resolution, faster neuronal activity indicators [43,44], higher-sensitivity channelrhodopsin [11], and faster volumetric imaging [45–47] are required. Faster indicators and volumetric imaging will reveal the different activation dynamics between cortical areas. Higher-sensitivity channelrhodopsin will enable our system to activate the target neurons in a single trial and to capture the activities of all neurons during the stimulation. In addition, we must accelerate the data analysis, enabling updating of the stimulation target according to ever-changing brain states [48,49]. Finally, several optogenetic probes, such as photo-convertible fluorescent proteins and light-switchable gene expression systems [50–52], can be employed in our system to elucidate the details of the involved neuronal ensembles.

Thus, with our method and further improvements, the research advantages provided by larval zebrafish can be fully exploited by manipulating the activity and molecular composition of arbitrarily selected neurons across the whole brain and monitoring the effects on brain-wide neuronal activities and behaviors.

Funding

Disclosures

The authors declare that there are no conflicts of interest related to this article.

References

1. M. Siegel, T. J. Buschman, and E. K. Miller, "Cortical information flow during flexible sensorimotor decisions," Science **348**(6241), 1352–1355 (2015).
2. T. W. Chen, N. Li, K. Daie, and K. Svoboda, "A map of anticipatory activity in mouse motor cortex," Neuron **94**(4), 866–879 (2017).
3. H. Makino, C. Ren, H. Liu, A. N. Kim, N. Kondapaneni, X. Liu, D. Kuzum, and T. Komiyama, "Transformation of cortex-wide emergent properties during motor learning," Neuron **94**(4), 880–890 (2017).
4. W. E. Allen, I. V. Kauvar, M. Z. Chen, E. B. Richman, S. J. Yang, K. Chan, V. Gradinaru, B. E. Deverman, L. Luo, and K. Deisseroth, "Global representations of goal-directed behavior in distinct cell types of mouse neocortex," Neuron **94**(4), 891–907.e6 (2017).
5. A. Muto, M. Ohkura, G. Abe, J. Nakai, and K. Kawakami, "Real-time visualization of neuronal activity during perception," Curr. Biol. **23**(4), 307–311 (2013).
6. R. Portugues, C. E. Feierstein, F. Engert, and M. B. Orger, "Whole-brain activity maps reveal stereotyped, distributed networks for visuomotor behavior," Neuron **81**(6), 1328–1343 (2014).
7. J. L. Semmelhack, J. C. Donovan, T. R. Thiele, E. Kuehn, E. Laurell, and H. Baier, "A dedicated visual pathway for prey detection in larval zebrafish," eLife **3**, e04878 (2014).
8. M. B. Ahrens, J. M. Li, M. B. Orger, D. N. Robson, A. F. Schier, F. Engert, and R. Portugues, "Brain-wide neuronal dynamics during motor adaptation in zebrafish," Nature **485**(7399), 471–477 (2012).
9. T. W. Chen, T. J. Wardill, Y. Sun, S. R. Pulver, S. L. Renninger, A. Baohan, E. R. Schreiter, R. A. Kerr, M. B. Orger, V. Jayaraman, L. L. Looger, K. Svoboda, and D. S. Kim, "Ultrasensitive fluorescent proteins for imaging neuronal activity," Nature **499**(7458), 295–300 (2013).
10. N. C. Klapoetke, Y. Murata, S. S. Kim, S. R. Pulver, A. Birdsey-Benson, Y. K. Cho, T. K. Morimoto, A. S. Chuong, E. J. Carpenter, Z. Tian, J. Wang, Y. Xie, Z. Yan, Y. Zhang, B. Y. Chow, B. Surek, M. Melkonian, V. Jayaraman, M. Constantine-Paton, G. K. Wong, and E. S. Boyden, "Independent optical excitation of distinct neural populations," Nat. Methods **11**(3), 338–346 (2014).

11. K. Deisseroth, "Optogenetics: 10 years of microbial opsins in neuroscience," Nat. Neurosci. **18**(9), 1213–1225 (2015).
12. V. Emiliani, A. E. Cohen, K. Deisseroth, and M. Häusser, "All-optical interrogation of neural circuits," J. Neurosci. **35**(41), 13917–13926 (2015).
13. J. P. Rickgauer, K. Deisseroth, and D. W. Tank, "Simultaneous cellular-resolution optical perturbation and imaging of place cell firing fields," Nat. Neurosci. **17**(12), 1816–1824 (2014).
14. A. M. Packer, L. E. Russell, H. W. Dalgleish, and M. Häusser, "Simultaneous all-optical manipulation and recording of neural circuit activity with cellular resolution in vivo," Nat. Methods **12**(2), 140–146 (2015).
15. M. dal Maschio, J. C. Donovan, T. O. Helmbrecht, and H. Baier, "Linking neurons to network function and behavior by two-photon holographic optogenetics and volumetric imaging," Neuron **94**(4), 774–789.e5 (2017).
16. Z. V. Guo, A. C. Hart, and S. Ramanathan, "Optical interrogation of neural circuits in Caenorhabditis elegans," Nat. Methods **6**(12), 891–896 (2009).
17. E. Warp, G. Agarwal, C. Wyart, D. Friedmann, C. S. Oldfield, A. Conner, F. Del Bene, A. B. Arrenberg, H. Baier, and E. Y. Isacoff, "Emergence of patterned activity in the developing zebrafish spinal cord," Curr. Biol. **22**(2), 93–102 (2012).
18. P. Zhu, O. Fajardo, J. Shum, Y. P. Zhang Schärer, and R. W. Friedrich, "High-resolution optical control of spatiotemporal neuronal activity patterns in zebrafish using a digital micromirror device," Nat. Protoc. **7**(7), 1410–1425 (2012).
19. M. B. Ahrens, M. B. Orger, D. N. Robson, J. M. Li, and P. J. Keller, "Whole-brain functional imaging at cellular resolution using light-sheet microscopy," Nat. Methods **10**(5), 413–420 (2013).
20. T. Panier, S. A. Romano, R. Olive, T. Pietri, G. Sumbre, R. Candelier, and G. Debrégeas, "Fast functional imaging of multiple brain regions in intact zebrafish larvae using Selective Plane Illumination Microscopy," Front. Neural Circuits **7**, 65 (2013).
21. N. Vladimirov, Y. Mu, T. Kawashima, D. V. Bennett, C.-T. Yang, L. L. Looger, P. J. Keller, J. Freeman, and M. B. Ahrens, "Light-sheet functional imaging in fictively behaving zebrafish," Nat. Methods **11**(9), 883–884 (2014).
22. P. J. Keller and M. B. Ahrens, "Visualizing whole-brain activity and development at the single-cell level using light-sheet microscopy," Neuron **85**(3), 462–483 (2015).
23. Z. Yang, L. Mei, F. Xia, Q. Luo, L. Fu, and H. Gong, "Dual-slit confocal light sheet microscopy for in vivo whole-brain imaging of zebrafish," Biomed. Opt. Express **6**(5), 1797–1811 (2015).
24. C. H. Kim, E. Ueshima, O. Muraoka, H. Tanaka, S. Y. Yeo, T. L. Huh, and N. Miki, "Zebrafish elav/HuC homologue as a very early neuronal marker," Neurosci. Lett. **216**(2), 109–112 (1996).
25. R. Amo, H. Aizawa, M. Takahoko, M. Kobayashi, R. Takahashi, T. Aoki, and H. Okamoto, "Identification of the zebrafish ventral habenula as a homolog of the mammalian lateral habenula," J. Neurosci. **30**(4), 1566–1574 (2010).
26. T. N. deCarvalho, C. M. Akitake, C. Thisse, B. Thisse, and M. E. Halpern, "Aversive cues fail to activate fos expression in the asymmetric olfactory-habenula pathway of zebrafish," Front. Neural Circuits **7**, 98 (2013).
27. B. B. Zhang, Y. Y. Yao, H. F. Zhang, K. Kawakami, and J. L. Du, "Left habenula mediates light-preference behavior in zebrafish via an asymmetrical visual pathway," Neuron **93**(4), 914–928 (2017).
28. R. G. Northcutt, "Localization of neurons afferent to the optic tectum in Longnose Gars," J. Comp. Neurol. **204**(4), 325–335 (1982).
29. A. Niida and T. Ohono, "An extensive projection of fish dorsolateral tegmental cells to the optic tectum revealed by intra-axonal dye marking," Neurosci. Lett. **48**(3), 261–266 (1984).
30. D. B. Rye, C. B. Saper, H. J. Lee, and B. H. Wainer, "Pedunculopontine tegmental nucleus of the rat: cytoarchitecture, cytochemistry, and some extrapyramidal connections of the mesopontine tegmentum," J. Comp. Neurol. **259**(4), 483–528 (1987).
31. J. Cornwall, J. D. Cooper, and O. T. Phillipson, "Afferent and efferent connections of the laterodorsal tegmental nucleus in the rat," Brain Res. Bull. **25**(2), 271–284 (1990).
32. J. Yañez and R. Anadón, "Afferent and efferent connections of the habenula in the rainbow trout (Oncorhynchus mykiss): an indocarbocyanine dye (DiI) study," J. Comp. Neurol. **372**(4), 529–543 (1996).
33. E. Rink and M. F. Wullimann, "Connections of the ventral telencephalon (subpallium) in the zebrafish (Danio rerio)," Brain Res. **1011**(2), 206–220 (2004).
34. G. V. Di Prisco, E. Pearlstein, D. Le Ray, R. Robitaille, and R. Dubuc, "A cellular mechanism for the transformation of a sensory input into a motor command," J. Neurosci. **20**(21), 8169–8176 (2000).
35. E. Gahtan, P. Tanger, and H. Baier, "Visual prey capture in larval zebrafish is controlled by identified reticulospinal neurons downstream of the tectum," J. Neurosci. **25**(40), 9294–9303 (2005).
36. W. C. Wang and D. L. McLean, "Selective responses to tonic descending commands by temporal summation in a spinal motor pool," Neuron **83**(3), 708–721 (2014).
37. R. C. Eaton, R. A. Bombardieri, and D. L. Meyer, "The Mauthner-initiated startle response in teleost fish," J. Exp. Biol. **66**(1), 65–81 (1977).
38. Y. Mu, X. Q. Li, B. Zhang, and J. L. Du, "Visual input modulates audiomotor function via hypothalamic dopaminergic neurons through a cooperative mechanism," Neuron **75**(4), 688–699 (2012).
39. A. M. B. Lacoste, D. Schoppik, D. N. Robson, M. Haesemeyer, R. Portugues, J. M. Li, O. Randlett, C. L. Wee, F. Engert, and A. F. Schier, "A convergent and essential interneuron pathway for Mauthner-cell-mediated escapes," Curr. Biol. **25**(11), 1526–1534 (2015).

40. A. M. Packer, B. Roska, and M. Häusser, "Targeting neurons and photons for optogenetics," Nat. Neurosci. **16**(7), 805–815 (2013).

41. S. Peron and K. Svoboda, "From cudgel to scalpel: toward precise neural control with optogenetics," Nat. Methods **8**(1), 30–34 (2011).

42. V. Szabo, C. Ventalon, V. De Sars, J. Bradley, and V. Emiliani, "Spatially selective holographic photoactivation and functional fluorescence imaging in freely behaving mice with a fiberscope," Neuron **84**(6), 1157–1169 (2014).

43. Y. Gong, C. Huang, J. Z. Li, B. F. Grewe, Y. Zhang, S. Eismann, and M. J. Schnitzer, "High-speed recording of neural spikes in awake mice and flies with a fluorescent voltage sensor," Science **350**(6266), 1361–1366 (2015).

44. F. St-Pierre, J. D. Marshall, Y. Yang, Y. Gong, M. J. Schnitzer, and M. Z. Lin, "High-fidelity optical reporting of neuronal electrical activity with an ultrafast fluorescent voltage sensor," Nat. Neurosci. **17**(6), 884–889 (2014).

45. R. Prevedel, Y.-G. Yoon, M. Hoffmann, N. Pak, G. Wetzstein, S. Kato, T. Schrödel, R. Raskar, M. Zimmer, E. S. Boyden, and A. Vaziri, "Simultaneous whole-animal 3D imaging of neuronal activity using light-field microscopy," Nat. Methods **11**(7), 727–730 (2014).

46. L. Cong, Z. Wang, Y. Chai, W. Hang, C. Shang, W. Yang, L. Bai, J. Du, K. Wang, and Q. Wen, "Rapid whole brain imaging of neural activity in freely behaving larval zebrafish (Danio rerio)," eLife **6**, e28158 (2017).

47. D. H. Kim, J. Kim, J. C. Marques, A. Grama, D. G. C. Hildebrand, W. Gu, J. M. Li, and D. N. Robson, "Pan-neuronal calcium imaging with cellular resolution in freely swimming zebrafish," Nat. Methods **14**(11), 1107–1114 (2017).

48. L. Grosenick, J. H. Marshel, and K. Deisseroth, "Closed-loop and activity-guided optogenetic control," Neuron **86**(1), 106–139 (2015).

49. C. M. Niell and M. P. Stryker, "Modulation of visual responses by behavioral state in mouse visual cortex," Neuron **65**(4), 472–479 (2010).

50. S. Shimizu-Sato, E. Huq, J. M. Tepperman, and P. H. Quail, "A light-switchable gene promoter system," Nat. Biotechnol. **20**(10), 1041–1044 (2002).

51. E. A. Naumann, J. E. Fitzgerald, T. W. Dunn, J. Rihel, H. Sompolinsky, and F. Engert, "From whole-brain data to functional circuit models: the zebrafish optomotor response," Cell **167**(4), 947–960 (2016).

52. D. Förster, M. Dal Maschio, E. Laurell, and H. Baier, "An optogenetic toolbox for unbiased discovery of functionally connected cells in neural circuits," Nat. Commun. **8**(1), 116 (2017).